X

A 3D Graph-Cut based Algorithm for Evaluating Carotid Plaque Echogenicity and Texture

José C. R. Seabra & João M. R. Sanches
Instituto de Sistemas e Robótica, Instituto Superior Técnico
Universidade Técnica de Lisboa
Portugal

1. Introduction

Carotid atherosclerosis is the main cause of brain stroke, which is one of the most common neurological diseases in western countries. A distinguishing feature of this disease is plaque formation owing to progressive sub-endotelial accumulation of lipid, protein, cellular waste products, calcium and other substances in medium and large-sized blood vessel walls.
Plaques can grow large enough to significantly reduce the blood's flow through particular arteries such as the carotid arteries, leading to what is commonly designated as *stenosis*. However, most of the damage occurs when they become fragile and rupture. Plaques that rupture cause blood clots to form and travel along circulation possibly blocking smaller vessel ahead. If it blocks a blood vessel that feeds the brain, it causes a *brain stroke*.
The degree of stenosis is often pointed as the most significant clinical indicator of stroke risk and it was until recently the most critical criterion used to determine a surgical intervention (Consensus Group, 1995), together with age, health and patient's clinical history.
The benefit of surgery for plaque removal, termed *endarterectomy*, is clearly demonstrated for patients presenting high degree of *stenosis* (more than 60%) (Consensus Group, 1995). It was also demonstrated, however, that patients on medical treatment remained free of symptoms for a long-time period despite the presence of considerable stenotic lesions. This advises for investigating and employing other clinical features for the evaluation of the risk of plaque rupture (Barnett et al, 2002; Elatrozy et al, 1998).
Currently, there are accurate methods to assess the disease severity based on (Wintermark et al, 2008) or MRI (Saam et al, 2007). However their application is expensive, time consuming and requires equipment which is not yet available and accessible in most clinical facilities. On the other hand, 2D ultrasound is widely available and provides real time data-acquisition and visualization, so it has been so far the preferred technique in the diagnosis and monitoring of the disease.
Plaque echo-morphology assessed through B-mode 2D ultrasound plays nowadays an important role in the evaluation of stroke risk in the scope of the atherosclerotic disease.
In the literature (Kyriacou et al, 2009; Mougiakakou et al, 2007; Sztajzel et al, 2005) several methods are described aiming at assessing the risk of plaque rupture based on the average echogenicity and texture characterization extracted from 2D ultrasound images of carotid

plaques. Current diagnostic methods present, however, two main flaws. First, the computation of echo-morphological features is usually affected by inaccuracy and subjectivity associated with data acquisition and operator dependent image selection. On the other hand, the analysis of overall echogenicity and texture of the carotid plaque, encoded by means of an averaged measure of pixel intensity values and variance, respectively, may not be accurate enough in many cases, namely when plaques are heterogeneous or present significant hypoechogenic regions. An overall measure of echogenicity or texture is incomplete and does not reveal unstable foci inside the plaque which should be considered for a correct evaluation of the risk of plaque rupture. Moreover, most methods for characterization of plaque echo-morphology do not usually take into account the *speckle* noise which can significantly corrupt the ultrasound data.

Fundamentals of plaque echo-morphology, including the most noticeable clinical indicators and methods for echo-morphological analysis are addressed in Section II.

Section III delineates a more robust, objective and complete framework proposed by the authors. The proposed methodology is based on 3D ultrasound which considers all the information contained on the carotids and plaque structures without depending on a subjective selection of a particular 2D image for diagnosis. To accomplish this task, a semi-automatic 3D reconstruction (de-noising) of the plaque is performed and features related to echogenicity and texture are computed. A procedure for investigating different textural contents and patterns is here investigated by extracting features from estimated speckle fields.

The proposed technique provides diagnostic views not usually accessible via conventional techniques and a new set of features useful for accurately study the plaque morphology. To complement this clinical information, it is suggested that the presence of vulnerable regions inside the plaques, together with their extension and location, may play an important role in the early assessment of stroke risk. These vulnerable regions are defined by low echogenicity (intensity) and high heterogeneity, quantified by reference values mentioned in the literature (El-Barghouty et al, 1996; Elatrozy et al, 1998; Sztajzel et al, 2005).

For this purpose, a 3D Graph-Cuts based algorithm is described to segment/label the most vulnerable (unstable) regions inside the carotid plaque. The algorithm allows to binary segment the data by minimizing an energy function that uses spatial correlation among neighboring pixels/voxels to remove small misclassified regions. The algorithm, highly efficient from a computational point of view, is able to find the global minimizer of this huge combinatorial optimization problem.

The work described by the authors presents an improvement of the 2D based classical approach in the analysis of carotid plaques. This 3D based methdology, together with new risk indicators and a local labelling of unstable foci within the plaque volume is more robust and reduces the subjectivity and operator dependency of the classical method.

Experimental results presented in Section IV show that this labelling procedure is less noisier and favours clustering, being more meaningful from a clinical point of view than the one obtained with simple thresholding.

Section V concludes the chapter and points some potentially meaningful research lines in the context of characterization of carotid plaques.

2. Fundamentals of Plaque Echo-Morphology

Besides the classical indicators such as the degree of *stenosis*, plaque morphology has been pointed as a relevant indicator for assessing the risk of plaque rupture.
2D *B-mode* (Brightness mode) ultrasound is a widely used imaging tool to assess the degree of *stenosis* as well as the plaque morphology. The two most important parameters to characterize the plaque morphology are its echogenicity and texture (Elatrozy et al, 1998).
The echogenicity is evaluated from the image intensities. A region is called *hypoechogenic* if it appears dark in the image and *hyperechogenic* if it appears bright. Concerning the texture it is usually classified as homogeneous or heterogeneous.
Several studies were pursued to statistically characterize the morphology of carotid plaques in 2D ultrasound (Sztajzel et al, 2005). The *Gray-Scale Median* (GSM) is one of the most important indicators considered on plaque diagnosis and is generally used to classify plaques as *hypoechogenic* (GSM < 32) or *hyperechogenic* (GSM > 32) (Pedro et al, 2002). The total percentage of *hypoechogenic* pixels (P40), defined as the percentage of pixels with gray levels below 40, is also an important measure for the characterization of plaque echogenicity. In fact, multiple regression analysis (Sztajzel et al, 2005) has revealed that the GSM and the P40 are the most significant variables related with the presence of symptoms. Recently, an activity index aiming at quantifying the risk of stroke (Pedro et al, 2002) has been proposed. This overall index merges several indicators, such as, plaque overall texture, degree of *stenosis*, global *echogenicity* and location of *hypoechogenic* sites across the plaque.
A vulnerable plaque is associated with thinning of the fibrous cap and infiltration of inflammatory cells that lead to plaque rupture. Studies which established a correlation between quantitative analysis based on ultrasound B-mode images and histology (Baroncini et al, 2006) have suggested that *hypoechogenic* regions have more lipid and hemorrhage, indicating inflammatory activity and therefore instability. Conversely, *hyperechogenic* regions are associated with the presence of stable components. Therefore, the location and extension of vulnerable regions throughout the carotid plaque could be a sensitive and relevant marker of stroke risk. Analysis of global information about plaque morphology, despite its unquestionable usefulness, may not be accurate enough in many cases, namely, when plaques are *heterogeneous* or present significant *hypoechogenic* regions. An overall measure of *echogenicity* or texture is incomplete and does not reveal unstable *foci* inside the plaque which may be threatening.

3. Methods

Tissue and organ reconstructions are generally performed by use of two rendering techniques: surface and volume rendering. Surface rendering (Meairs & Hennerici, 1999; Schminke et al, 2000) can be used to extract the bifurcation walls of carotid arteries and quantify the degree of *stenosis* as well as assess the plaque volume. A volume rendering approach (Bullitt & Aylward, 2002) is often used to reconstruct a particular volume of interest from which echo-morphological or textural analysis can be further performed. Here, a combination of the two approaches is used. First, volume renderings are obtained from sets of 2D ultrasound images of the carotid artery. The regions corresponding to atherosclerotic plaques are visually detected in several cross-sections taken from the obtained volume and then segmented using semi-automatic segmentation methods, e.g. active contours (Xu & Prince, 1998) guided by experienced physicians. Surface rendering

employs the interpolation of these contours providing a three-dimensional representation of the plaque.
The data used in this study consists of 3 sets of n = 100 nearly parallel cross-sections of the carotid artery, from 3 distinct patients, acquired near the bifurcation where plaque formation is more frequent.
The reconstruction algorithm proposed by the authors in (Seabra et al, 2009) is used. The acquisition protocol proposed in the referred publication does not require any additional equipment but the conventional 2D ultrasound scanner available in most medical facilities.
Ultrasound images are corrupted by *speckle*, which makes data visualization and interpretation often a challenging task. The method used here to compute the 3D morphology of the *region of interest* (ROI) containing the carotid plaque is composed of two main steps: i) de-noising and ii) reconstruction. In the first step the ultrasound images, assumed parallel and evenly spaced, are de-noised with the method described in (Seabra & Sanches, 2008). In the second step, these de-noised images are interpolated to estimate the 3D region of interest containing the plaque.

3.1 De-noising

The de-noising algorithm, designed in a Bayesian framework, takes into account the RF signal compression performed by the ultrasound equipment which changes the distribution of the raw data provided by the ultrasound probe known to be, under particular conditions, Rayleigh distributed (Eltoft, 2006; Michailovich & Tannenbaum, 2006).
Here, the following *Log-compression* model is considered

$$z_{i,j} = a\log(y_{i,j} + 1) + b\,, \tag{1}$$

where a and b are the parameters to be estimated and account for the contrast and brightness adjustments, respectively, performed by the physician during the medical exam, $z_{i,j}$ are the noiseless pixel intensities of the compressed image and $y_{i,j}$ are the pixels of the corresponding de-compressed image that are assumed to be Rayleigh distributed . The parameters a and b, estimated directly from the observed noisy images as described in (Seabra & Sanches, 2008), are used to invert the transformation (1) and obtain an estimation of the original RF Rayleigh distributed data,

$$y_{i,j} = e^{\frac{z_{i,j}-b}{a}}\,. \tag{2}$$

In Fig. 1 it is illustrated the effect of the parameter x on the shape of the Rayleigh PDF. It is also shown how the *Log-Compression Law*, which is an approximation of the ultrasound processing block, changes the Rayleigh distribution of the RF data.
The de-noising algorithm, designed in a Bayesian framework with the *Maximum a Posteriori* (MAP) criterion may be formulated as folllows

$$\hat{X} = \arg\min_{X} E(X, Y)\,, \tag{3}$$

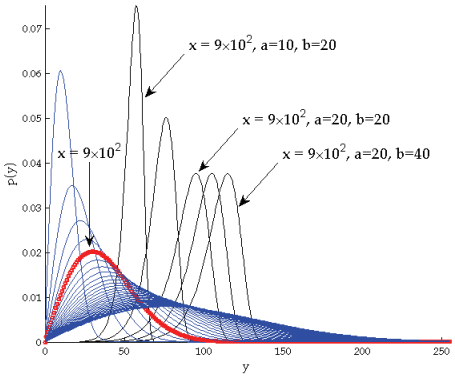

Fig. 1. Rayleigh probability density functions (PDF's) for parameters x from 10^2 to 6×10^3 in steps of 10^2, generated according to (6). PDF's using $x = 9\times10^2$ and different values of a and b illustrate the significant change that occurs on the original Rayleigh distribution.

where $X = \{x_{i,j}\}$ is the denoised image and $Y = \{y_{i,j}\}$ is the estimated RF signal obtained after inverting (1). The energy function is

$$E(X,Y) = E_Y(X,Y) + E_X(X), \tag{4}$$

where $E_Y(X,Y)$, called *data fidelity term*, pushes the solution toward the data Y and $E_X(X)$, called *prior term*, regularizes the solution. By assuming statistical independence of the observations the data fidelity term is

$$E_Y(X,Y) = \log \prod_{i,j} p(y_{i,j|} \mid x_{i,j|}), \tag{5}$$

where

$$p(y_{i,j} \mid x_{i,j}) = (y_{i,j}/x_{i,j})e^{-y_{i,j}/(2x_{i,j})} \tag{6}$$

is the Rayleigh distribution with parameter $x_{i,j}$. The *prior term* is

$$E_X(X) = -\log p(X), \tag{7}$$

By assuming that X is a *Markov Random Field* (MRF),

$$p(X) = \frac{1}{\Omega} e^{-\alpha \sum_{i,j} V_{i,j}}, \tag{8}$$

is a Gibbs distribution where Ω is the partition function, α is the prior parameter and $V_{i,j}$ are the potential functions associated with the *cliques* of the MRF, X (Geman & Geman, 1984). Therefore, the *prior term* $E_X(X) = \alpha \sum_{i,j} V_{i,j} + C$ is the so-called Gibbs energy that is here proportional to the *Total Variation* (TV) of X (Vogel & Oman, 1998) where

$$V_{i,j} = \sqrt{(x_{i,j} - x_{i-1,j})^2 + (x_{i,j} - x_{i,j-1})^2} \tag{9}$$

are the magnitudes of the discrete gradient of X at the locations (i, j). These functions are edge preserving because, in relative terms, they penalize more small differences between neighbouring pixels due to noise than large differences due to anatomical transitions.
Details on the estimation procedure are described in (Seabra et al, 2008; Seabra et al, 2009) and an example to illustrate de application of the algorithm is displayed in Fig. 2.
In this step the speckle field is also estimated from the estimated RF and denoised images. The speckle noise corrupting the ultrasound images is multiplicative in the sense that its variance depends on the underlying signal $x_{i,j}$. The image formation model may be formulated as follows

$$y_{i,j} = \eta_{i,j} \sqrt{x_{i,j}}\ , \tag{10}$$

where $x_{i,j}$ is the de-speckled pixel intensity at location (i, j) and $y_{i,j}$ and $\eta_{i,j}$ the corresponding pixel intensities of the RF image and the speckle field, respectively.
In this model, the speckle field $\eta = \{\eta_{i,j}\}$ is independent of the signal as occurs in a common *Additive White Gaussian Noise* (AWGN) model where the noisy pixels, $Y = X + \eta$, are the sum of two independent terms, X and η.
In the case of multiplicative noise the operation is not additive but multiplicative as shown in (10). The distribution of η is

$$p(\eta) = \left|\frac{dy}{d\eta}\right| p(y) = \eta e^{-\frac{\eta^2}{2}}, \qquad \eta \geq 0\,, \tag{11}$$

which is a unit parameter Rayleigh distribution independent of x. The computation of the speckle field, η, is performed from the estimated/observed RF noisy image, Y, and from the de-speckled field, X,

$$\eta_{ij} = \frac{y_{ij}}{\sqrt{x_{ij}}}\,. \tag{12}$$

Given this, the authors argue that the de-noising procedure may have a two-fold purpose: first, it can provide clearer ultrasound images for better visualization of the structures in the image and also a speckle field. The estimated speckle field may be used to perform a more

accurate and objective textural analysis and differentiate between tissues having different densities and patterns.

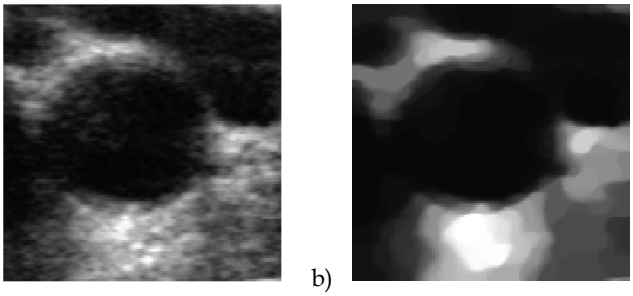

a) b)

Fig. 2. Original ultrasound (a) and de-noised (b) images.

3.2 Reconstruction

The 3D reconstruction of the ROI containing the plaque aims at estimating a 3D field, $F = \{f_p\}$ from the denoised images computed in the previous step, $X^t = \{x^t_{i,j}\}$, where t denotes the t^{th} image in the sequence of evenly spaced parallel ultrasound cross sections and $p = (i, j, k)$ represents a node index in the 3D matrix F. The node locations of F, f_p, and the locations of the pixels of X^t, $x^t_{i,j}$ do not necessarily match and therefore an interpolation process is required. Furthermore, some nodes may not be observed which poses a problem of missing data. The following approach is proposed.

Let us consider each voxel as the cubic region, centred at the location of the node f_p, μ_p with dimensions $(\Delta_1, \Delta_2, \Delta_3)$ and the locations of the denoised pixels $x^t_{i,j}$, $\tau^t_{i,j}$. Let $\Sigma_p = \{x^t_{r,l} : \tau^t_{r,l} \in S_{\Delta_1,\Delta_2,\Delta_3}(\mu_p)\}$ be the set of all pixels inside the neighbourhood (voxel) $S_{\Delta_1,\Delta_2,\Delta_3}(\mu_p)$ of the node f_p displayed in Fig. 3.

In a first step a 3D volume, $Z = \{z_p\}$ with the same dimensions of X, is computed where each element $z_p = \langle \Sigma_p \rangle$ is the weighted mean of the set Σ_p where the weights are the normalized distances of the pixel locations to the centre of the voxel, $z_p = (\sum_r \|\tau_r - \mu_p\| x_r) / (\sum_r \|\tau_r - \mu_p\|)$ where τ_r denotes the location of the r^{th} pixel within the set Σ_p. Therefore, each element of Z contains the average intensity of the pixels within the voxel. However, some elements of Z may be undefined when there are no observations (pixels) inside the voxel. In this case an interpolation is needed. This missing data problem may be solved by minimizing the following energy function

$$E(F, Z) = \sum_p \left[n_p (f_p - z_p)^2 + \alpha g_p^2 \right], \tag{13}$$

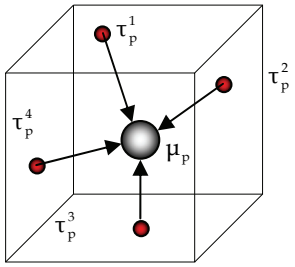

Fig. 3. Voxel representation associated with the node f_p (grey), located at μ_p, and several image pixels, at locations τ_p^r in its neighbourhood (red).

where $p = (i, j, k)$ and $g_p = \sqrt{(f_{i,j,k} - f_{i-1,j,k})^2 + (f_{i,j,k} - f_{i,j-1,k})^2 + (f_{i,j,k} - f_{i,j,k-1})^2}$ is the gradient magnitude of F at the voxel p and n_p is the number of observations (pixels) associated with the voxel p. The minimization of (13) may be iteratively solved by optimizing with respect to one unknown at a time, which leads to the following recursion

$$f_p^t = \beta(n_p) z_p + (1 - \beta(n_p)) \bar{f}_p^{t-1}, \tag{14}$$

where $()^t$ denotes the iteration t, $\bar{f}_p^{t-1}$ denotes the mean value of the neighbours of f_p computed in the iteration $t-1$, n_p is the number of image pixels inside the voxel and $\beta(n_p) = \dfrac{n_p}{n_p + \alpha N_v}$ is a regularization parameter function, displayed in Fig. 4, depending on n_p, on the number of neighbours of f_p, $N_v = 6$, and on the tuning parameter α.

The equation (13) reveals the underlying interpolation mechanism performed during the minimization of the energy function (12). Each new estimates of F, F^t, depends on the previous one, F^{t-1}, and on the field of the mean pixel intensities, Z, computed in the previous step. As large is the number of pixels associated with a given voxel, n_p, as close to one is the parameter β, which means, in the limit, $f_p^t \approx z_p$. Conversely, a small number of observed pixels leads to small values of β, which means that the new estimates of f_p^t is computed part from z_p and part from the neighbours, $\bar{f}_p^{t-1}$ computed in the previous iteration. In the limit, when no observations are available, $\beta = 0$, and the new estimate is $f_p^t = \bar{f}_p^{t-1}$, that is, it is equal to the mean intensity of its neighbours. This method adopts the following strategy: when a large number of observed pixels are available for a given voxel its value is mainly computed from Z and when the number of observations is small or even zeros the estimates of f_p is obtained mainly from the neighbourhood.

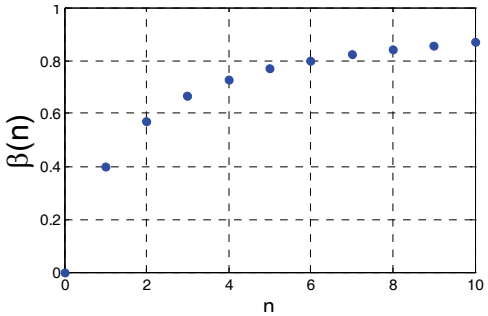

Fig. 4. Regularization parameter function depending on the number of observed pixels.

3.3 Feature Extraction

The volume field F describes the value of the Rayleigh parameter across the volume of interest containing the carotid plaque and it may be used to compute local intensity and textural indicators that characterize the components and tissues of the plaque.

Traditionally, plaque characterization is based on statistics computed from the observed noisy pixels. Here, instead of computing these indicators from the noisy data, the characterization is based on statistical estimators depending on F containing the Rayleigh parameters associated with the RF estimated data throughout the whole plaque.

The echogenicity and texture measures are derived from statistical estimators for the mean $f_{\mu}(p)$, median (GSM) $f_{v}(p)$, standard deviation $f_{\sigma}(p)$ and percentile 40 $f_{P40}(p)$ depending on f_P where $p=(i,j,k)$. These statistics, derived form the Rayleigh distribution (Abramowitz et al., 1972), are given by

$$\begin{cases} f_{\mu}(p)=\sqrt{\dfrac{f_P\pi}{2}} \\ f_{v}(p)=\sqrt{2\log(2)f_P} \\ f_{\sigma}(x)=\sqrt{\dfrac{4-\pi}{2}}f_P \\ f_{P40}(x)=1-e^{-\frac{40^2}{2f_P}} \end{cases} \tag{15}$$

Four 3D matrices are build containing the values of these estimators at each location $p=(i,j,k)$, F_{μ}, F_{v}, F_{σ} and F_{P40}. By averaging the elements of these 3D matrices, global indicators about the plaque can be computed. The global ecogenecity of the plaque is the mean of F_{μ}, $\langle F_{\mu}\rangle$ and the global textural characterization is the average of the other matrices, $\langle F_{v}\rangle$, $\langle F_{\sigma}\rangle$ and $\langle F_{P40}\rangle$.

3.4 Local Characterization by use of Graph-Cuts

The global characterization of carotid plaques, described in the previous section by averaging the statistical estimators in (15), despite its unquestionable usefulness may not be

enough for a correct assessment of plaque vulnerability, especially in cases where the plaque is significantly heterogeneous or is plagued by artefacts.

Here a local based characterization approach is proposed. The goal is to use the statistical estimators (15) to assess the risk of plaque rupture on a local basis. The method allows to identify sites within the plaque whose features (hypoechogenicity and heterogeneity) point towards potential foci of vulnerability.

The classification of the plaque at each location $p = (i, j, k)$ can be made by thresholding where the elements of the matrices F_μ, F_v, F_σ and F_{P40} are binarized according to a threshold defined by the physician (El-Barghouty et al, 1996; Pedro et al, 2002). The resulting 3D maps characterize locally the plaque with respect to each indicator.

This thresholding algorithm is simple but does not take into account spatial correlation between neighbouring nodes because the process is performed in a voxel-by-voxel basis. Here, a more sophisticated and accurate method is used where the labeling procedure considers the intensity value of the statistical function at location p and also the values of its neighbouring nodes. The spatial correlation is introduced in order to reduce the misclassification rate by assuming that the plaque is composed of homogeneous regions separated by abrupt transitions. This assumption is acceptable from an anatomical perspective and is usually adopted in de-noising and de-blurring algorithms on medical imaging.

Let f_p be the estimated value of F at the p^{th} node. The labeled maps, L_τ with $\tau = \{\mu, v, \sigma, P_{40}\}$, are defined on a plane-by-plane basis, *i.e.* each plane is labeled independently of the others. The segmentation is binary, which means $L(p) \in \{0,1\}$ where $L(p)$ is the p^{th} node of L.

The labeling procedure of the whole volume is performed in three steps, as depicted in Fig. 5: (i) all stacked planes along the vertical direction are independently labeled, (ii) all stacked planes along the horizontal direction are independently labeled, and (iii) both volumes obtained in the previous steps, L^v and L^h, are fused by making $L = L^v \otimes L^h$ where $\otimes$ denotes the element wise Boolean product.

The labeling process of each plane is performed by solving the following optimization problem

$$L_\tau = \arg\min_L E(F_\tau, L), \tag{16}$$

with the energy function being given by

$$E_\tau(F_\tau, L) = \sum_p (\lambda_\tau - f_p)(2L(p) - 1) + \theta \sum_p \frac{V(L(p), L(p_v)) + V(L(p), L(p_h))}{\tilde{g}_p}, \tag{17}$$

where λ_τ is the threshold associated with the indicator τ and θ is a parameter to tune the strength of smoothness, $\tilde{g}_p$ is the normalized gradient at location p, and p_v and p_h are the locations of the causal vertical and horizontal neighbours of the p^{th} node. $V(l_1, l_2)$ is a penalization function defined as follows

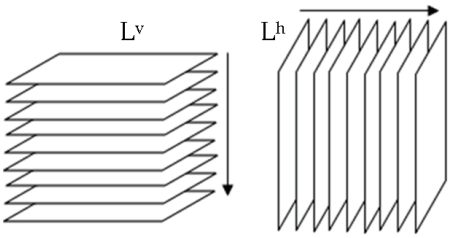

Fig. 5. Labeling procedure performed on a plane by plane basis in two steps, providing L^v and L^h.

$$V(l_1, l_2) = \begin{cases} 0 & l_1 = l_2 \\ 1 & l_1 \neq l_2 \end{cases}. \tag{18}$$

The energy function is composed of two terms: the first called *data term* and the second called *regularization term*. The first forces the classification to be $L(p) = 1$ when $f_p \geq \lambda_\tau$ because the corresponding term in the energy function (17) is smaller when compared with the one if $L(p) = 0$. The opposite occurs if $f_p < \lambda_\tau$. The second term forces the uniformity of the solution because the cost associated with uniform labels is smaller than with nonuniform ones (see (18)). In order to preserve the transitions the terms are divided by the normalized gradient magnitude of f_p, $\tilde{g}_p$. Therefore, when the gradient magnitude increases the regularization strength is reduced at that particular location.

The minimization of (17) formulated in (16) is a huge optimization task performed in the Ω^{NM} high dimensional space where $\Omega = \{0,1\}$ is the set of labels and N and M are the dimensions of the image.

In (Kolmogorov & Zabih, 2004) it is shown that several energy minimization problems in high dimensional discrete spaces can be efficiently solved by use of *Graph-Cuts* (Boykov, 2001) based algorithms. Opportunely, the energy function given in (17) belongs to this class of problems. The authors have designed a very fast and efficient algorithm to compute the global minimum of the energy function.

4. Experimental Results

In this section results from synthetic and real data are presented. Fig. 6 shows an example of application of the de-noising/reconstruction procedure, where a log-compressed ultrasound image and its corresponding estimated RF and de-speckled images are displayed. The log-compressed image was created by use of an echogenicity model of a synthetic plaque (regarded as a matrix of Rayleigh parameters) which was corrupted with Rayleigh noise and then processed according to the *Log-Compression Law* in (1). Given this result, the de-speckled image is regarded as a "clean" image, which is suitable for visualizing the underlying structures of interest. However, it may have a second interpretation: in fact, it represents a matrix of localwise estimated Rayleigh parameters.

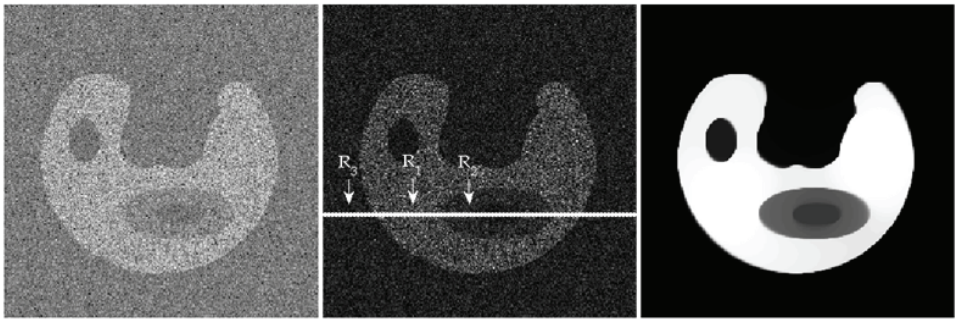

Fig. 6. Reconstruction procedure applied to a synthetic plaque. Log-compressed ultrasound image was used to estimate the RF image (middle) and its de-speckled version (right).

Fig. 7 displays the signal (pixel intensities) along a particular path (see Fig. 6). The signal is overlapped with the real Rayleigh parameters f_O which are part of the echogenicity model and the estimated ones, f_p, taken from the de-speckled image. This result clearly shows the ability of the de-speckling algorithm to reduce speckle while preserving the important edges of the image. The PDF's originated from the averaged values of the estimated Rayleigh parameters computed within portions R_1, R_2 and R_3 (see Fig. 6) were also computed. The histograms taken from each portion were overlapped with the PDF's to show the efficiency of the de-speckling algorithm on estimating correctly the Rayleigh parameters which model the data. Given this observation, the authors argue that the parameter of the Rayleigh distribution can be used to perform echo-morphological analysis of the tissue because it is a feature which clearly varies from one region to another in the image.

Although textural characterization is beyond the scope of this work, an example to illustrate the potential usefulness of the proposed methodology for textural characterization of the tissues, in particular of the carotid plaque, is here shown.

Fig. 8 shows results of the extraction of texture information from the speckle field of a synthetic image of a plaque presenting distinct pattern regions. Each image quadrant was convolved with a Gaussian mask of different size to simulate distinct smoothness levels. First, a de-speckled image is estimated where clearly the texture pattern was removed and only only echogenicity information from the plaque is visible. To retrieve potential significant information encoded in the speckle field a wavelet decomposition of the speckle image is computed to obtain the relative importance of approximation $E_a = E_a/(E_a + E_d)$ and detail $E_d = E_d/(E_a + E_d)$ energies. Fig. 8 (right) depicts the corresponding speckle field together with the computed approximation and detail energies. From the speckle field it is clearly visible that this image is not affected by the information encoded in the echogenicity (intensity) of the synthetic plaque, providing a suitable field for textural analysis. Higher percentages of approximation energies are obtained for the 2nd and 3rd image quadrants, which visibly correspond to smoother regions. On the other hand, detail values are particularly higher for the apparently noisier 4th quadrant.

In the remainder of this section, we present a set of four examples of application of the labeling method based on *Graph-Cuts* to characterize the echo-morphology of carotid plaques on a localwise basis, where two of them use synthetic data while the remaining two use real ultrasound data.

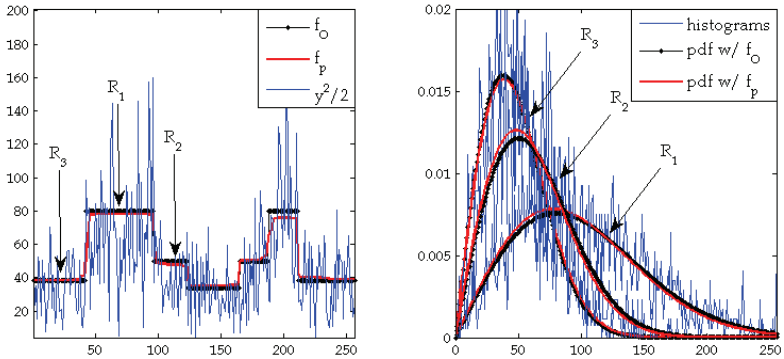

Fig. 7. Representation of a noisy signal (path extracted from Fig. 6) and the corresponding real f_O and estimated rayleigh parameters f_p. Histograms and PDF's originated with averaged values of rayleigh parameters extracted from R_1, R_2 and R_3.

Fig. 8. Extraction of texture information from the speckle field. (Left) Synthetic plaque, presenting regions with distinct texture patterns. (Middle) De-speckled image, where only anatomical information (echogenicity) is visible. (Right) Speckle field, from where approximation and detail energies were computed within each four regions by use of wavelet decomposition.

In the first example depicted in Fig. 9, the previously referred synthetic plaque was used to illustrate the *Graph-cuts* based labeling procedure. Here, the number of classes to detect given as input to the algorithm was *3* and the *data term* associated with the energy function to minimize was simply the image intensities. This simple example provides an illustration of how the *Graph-cuts* labeling algorithm is able to correctly label the different parts of the image.

The performance of the reconstruction and labeling algorithms was also evaluated with a "stack" of synthetically generated echogenicity models of the plaque. This time, the distinction between the different regions in the volume was made harder, and almost impossible after corruption with Rayleigh noise. Not only is the algorithm able to attenuate the speckle, providing a clearer reconstructed volume than the original one, but also allows us to identify the synthetically generated vulnerable hypoechogenic (dark) regions across the plaque. Moreover, the true rayleigh parameters associated with these regions (f_p = 20)

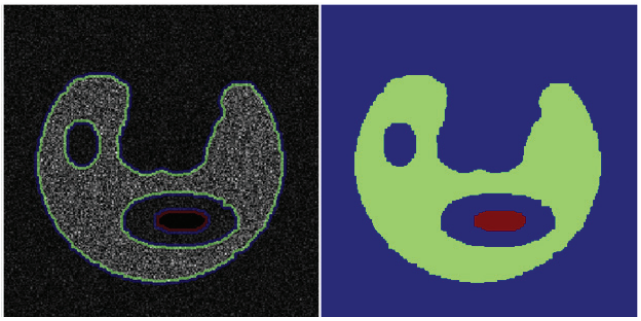

Fig. 9. Illustration of labeling based on *Graph-cuts* using a synthetic plaque corrupted with Rayleigh noise. The different regions are correctly labeled

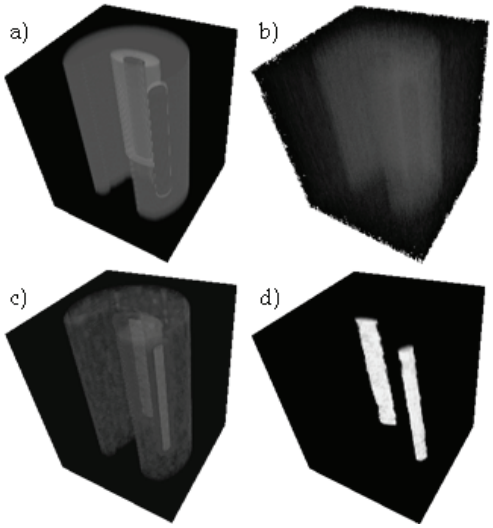

Fig. 10. Reconstruction and labeling using a 3D synthetic carotid plaque (a). Potentially vulnerable regions (two hypoechogenic (f_p = 20) and one mid-gray (f_p = 35) were created. (b) Carotid plaque, after being corrupted with Rayleigh noise. (c) De-speckled volume of the plaque, and (d) vulnerable sites were correctly labeled.

were correctly recovered by use of the labeling procedure based on *Graph-Cuts* where $f_\lambda = 20$ in (17).

In the third example, the labeling is performed in two longitudinal ultrasound images showing carotid plaques (see Fig. 11(a)). The segmented carotid plaques (see Fig. 11(b)) were characterized according to the labeling methods based on thresholding and *Graph-Cuts* (see Figs. 11(c-d)). In this example the original noisy images were used and a threshold value of 32 (gray-scale: 0−255) was employed to locally characterize the plaque echogenicity.

It is observed that a characterization based on a simple thresholding of the pixel intensities leads to labeled images with a great amount of noise, which are not realistic from a clinical point of view. In fact, physicians aim at identifying particular regions of vulnerability across

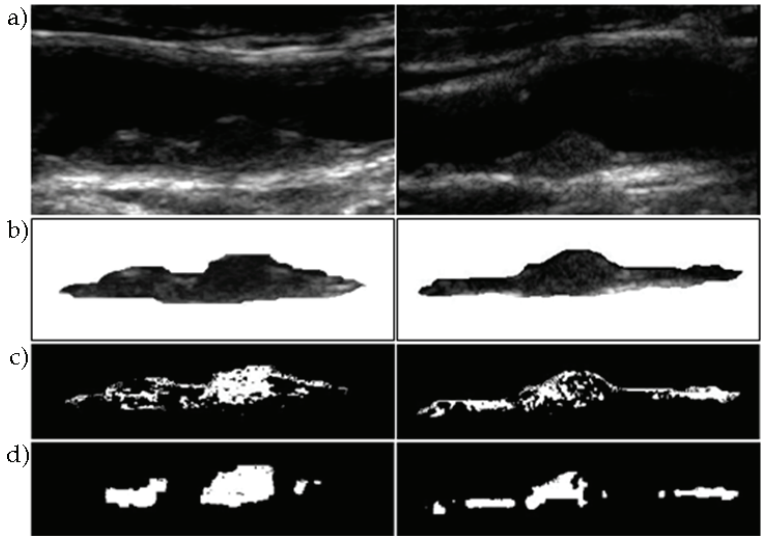

Fig. 11. Original ultrasound images (a) and segmented plaques (b). Labeling of plaques, by use of thresholding (c) and *Graph-Cuts* based methods (d).

the carotid plaques, where isolated or dispersed pixels (here termed outliers) are not expected to occur. It is verified (see Fig. 11(d)) that the labeling based on *Graph-Cuts* is less noisier and favors clustering, being more clinical meaningful than the one obtained with simple thresholding.

In the last example, three reconstructed real carotid plaques were locally characterized according to the previously described statistical indicators depending on the estimated parameters f_K of the Rayleigh distribution. The statistical estimators considered in this example are f_σ and f_{P40}.

Published studies (Pedro, 2002) in the carotid plaque characterization field suggest that hypoechogenic regions, corresponding to instability *foci*, have GSM < 32 and P40 > 43%.

Fig. 12 displays the labeling of potentially dangerous sites inside the plaque, using the two labeling methods described in this paper (thresholding and *Graph-Cuts*). It is again observed that the labeling using graph cuts allows to better discriminate the regions of interest across the carotid plaques.

Volumes labeled with *Graph-Cuts* appear less noisier than when the threshold method is used. This suggests that the use of graph-cuts may improve the characterization of carotid plaques, namely by providing a more appropriate identification and definition of unstable regions across the plaque. As it is pointed out (Pedro, 2002) the degree of extension of these unstable regions as well as their location throughout the plaque should be considered and used as markers of risk of plaque rupture and thus of stroke risk.

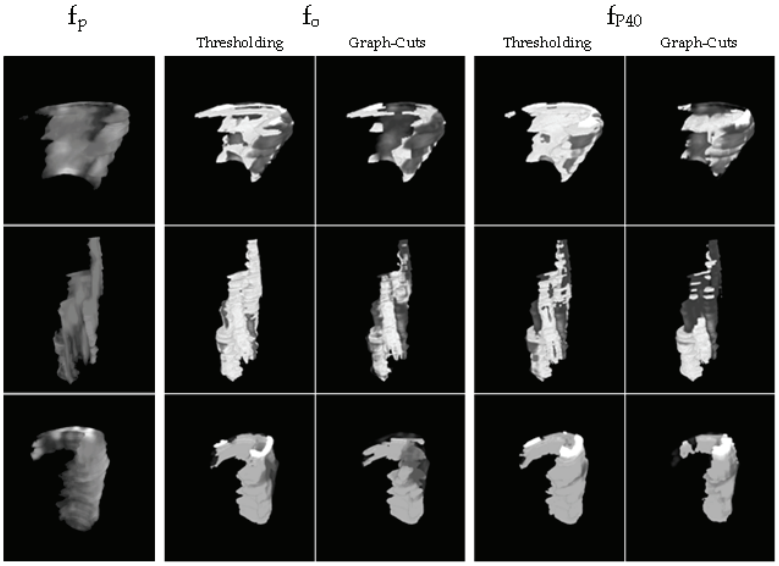

Fig. 12. Representation of echo-morphology of three different plaques encoded in f_p. Comparison of two labeling methods based on - thresholding and *Graph-Cuts* - computed with the local Rayleigh estimators of median $f_\sigma(x)$ and $f_{P40}(x)$.

5. Conclusions

Echo-morphology of atherosclerotic plaques as described by its echogenicity and texture assessed through ultrasound is nowadays considered a powerful indicator of stroke risk.

The authors present a robust, objective and complete methodology which consists of 3D reconstruction of the plaque and extraction of features related to plaque echogenicity and texture. It is shown that the Bayesian estimation method, employed for reconstruction/ de-noising is able to correctly estimate the parameters of the Rayleigh distribution and that these vary significantly from one tissue/ component to another.

An example showing the extraction of textural features from estimated speckle fields suggest its usefulness toward the textural characterization of the plaque tissues/ components.

Moreover, it is proposed a new approach to overcome the major limitations of an averaged characterization of the plaque composition by computing local indicators derived from Rayleigh statistics obtained from the noiseless reconstructed images/volumes containing the plaque. This method uses a fast computational labeling algorithm based on *Graph-cuts* to improve the segmentation of potential foci of instability across the plaques. Results show that the labeling method is less noisier and favors clustering, being more clinical meaningful than using simple thresholding.

6. References

Abramowitz, Milton; Stegun, Irene A., eds. (1972). *Handbook of Mathematical Functions with Formulas, Graphs, and Mathematical Tables*, New York: Dover Publications, ISBN 978-0-486-61272-0

Barnett, H.; Meldrum, H. & Eliasziw M. (2002). The appropriate use of carotid endarterectomy. *Canadian Medical Association*, No. 166, 1169–1179

Baroncini, L.; Filho, A.; Junior, L., A. Martins, and S. Ramos. (2006). Ultrasonic tissue characterization of vulnerable carotid plaque: correlation between videodensitometric method and histological examination. *Cardiovascular Ultrasound*, 4-32. Comparative Study

Boykov, Y.; Veksler, O. and Zabih, R. (2001). Fast approximate energy minimization via graph cuts. *IEEE Transactions on Pattern Analysis and Machine Intelligence*. Vol. 23, No. 11, 1222-1239

Bullitt, E. & Aylward, S. (2002). Volume rendering of segmented image objects. IEEE Transactions on Medical Imaging, Vol. 21, No. 8, 998-1002

Consensus Group (1995). Consensus statement on the management of patients with asymptomatic atherosclerotic carotid bifurcation lesions: international angiology. *International Angiology*, No. 14, 5–17

Elatrozy, T.; Nicolaides, A.; Tegos, T. & Griffin, M. (1998) The objective characterization of ultrasonic carotid plaque features. *European Journal of Vascular and Endovascular Surgery*, No. 16, 223–230

El-Barghouty, N.; Levine, T.; Ladva, S.; Flanagan, A. & Nicolaides, A. (1996). Histological verification of computerised carotid plaque characterisation. *European Journal of Endovascular Surgery.* Vol. 11, No. 4, 414–416

Eltoft, T. (2006). Modeling the amplitude statistics of ultrasonic images. *IEEE Transactions on Medical Imaging*, Vol. 25, No. 2, 229–240. Comparative Study

Geman, S. & Geman, D. (1984). Stochastic relaxation, Gibbs distributions, and the Bayesian restoration of images. *IEEE Transactions on Pattern Analysis and Machine Intelligence*, Vol. 6, No. 6, 721–741

Kolmogorov, V.; and Zabih, R. (2004). What energy functions can be minimized via graph cuts?. *IEEE Transactions on Pattern Analysis and Machine Intelligence*. Vol. 26, No. 2, 147–159

Kyriacou, E.; Pattichis, M.; Pattichis, C.; Mavrommatis, A.; Christodoulou, C.; Kakkos, S. & Nicolaides, A. (2009). Classification of atherosclerotic carotid plaques using morphological analysis on ultrasound images. *Applied Intelligence*, Vol. 30, No. 1, 3-23

Meairs, S. & Hennerici, M. (1999). Four-dimensional ultrasonographic characterization of plaque surface motion in patients with symptomatic and asymptomatic carotid artery stenosis. *Stroke*, Vol. 30, 1807–1813

Michailovich, O. & Tannenbaum, A. (2006). Despeckling of medical ultrasound images. *IEEE Transactions on Ultrasonics, Ferroelectrics, and Frequency Control*. Vol. 53, No. 1, 64-78

Mougiakakou, S.; Golemati, S.; Gousias, I.; Nicolaides, A. & Nikita, K. (2007). Computer-aided diagnosis of carotid atherosclerosis based on ultrasound image statistics, laws' texture and neural networks. *Ultrasound in Medicine and Biology*, Vol. 33, No. 1, 26-36

Pedro, L.; Fernandes, J.; Pedro, M.; Gonçalves, I. & Dias, N. (2002). Ultrasonographic risk score of carotid plaques. *European Journal of Vascular and Endovascular Surgery*, Vol. 24, 492–498

Saam, T.; Yuan, C.; Chu, B.; Takaya, N.; Underhill, H.; Cai, J.; Tran, N.; Polissar, N.; Neradilek, B.; Jarvik, G.; Isaac, C.; Garden, G.; Maravilla, K.; Hashimoto, B. & Hatsukami, T. (2007) Predictors of carotid atherosclerotic plaque progression as measured by noninvasive magnetic resonance imaging. *Atherosclerosis*, Vol. 194, No. 2, Pages 34-42

Schminke, U.; Motsch, L.; Hilker, L. & Kessler, C. (2000). Three-dimensional ultrasound observation of carotid artery plaque ulceration. *Stroke*, Vol. 31, No. 7, 1651–1655

Seabra, J. & Sanches, J. (2008) Modeling Log-Compressed Ultrasound Images for Radio Frequency Signal Recovery, *Proceedings of the 30th International Conference of the IEEE Engineering in Medicine and Biology Society,* 426-429, Vancouver, Canada, Aug 2008

Seabra, J.; Xavier, J. & Sanches, J. (2008). Convex ultrasound image reconstruction with log-Euclidean priors, *Proceedings of the 30th International Conference of the IEEE Engineering in Medicine and Biology Society,* 435-438, Vancouver, Canada, Aug 2008

Seabra, J.; Pedro, L.; Fernandes, J. & Sanches, J. (2009) A 3D Ultrasound-Based Framework to Characterize the Echo-Morphology of Carotid Plaques. *IEEE Transactions on Biomedical Engineering* [ahead of print]

Sztajzel, R.; Momjian, S.; Momjian-Mayor, I.; Murith, N. & Djebaili, K. (2005). Stratified gray-scale median analysis and color mapping of the carotid plaque: correlation with endarterectomy specimen histology of 28 patients. *Stroke*, Vol. 36, No. 4, 741–745

Vogel, C. and & Oman, M. (1998). Fast, robust total variation-based reconstruction of noisy, blurred images. *IEEE Transactions on Image Processing,* Vol.7, No. 6, 813-824

Wintermark, M.; Jawadi, S.; Rapp, J.; Tihan, T.; Tong, E.; Glidden, D.; Abedin, S.; Schaeffer, S.; Acevedo-Bolton, G.; Boudignon, B.; Orwoll, B.; Pan, X. & Saloner, D. (2008) High-Resolution CT Imaging of Carotid Artery Atherosclerotic Plaques. *American Journal of Neuroradiology*, Vol. 29, 875-882

Xu, C. & Prince, J. (1998). Snakes, shapes, and gradient vector flow. *IEEE Transactions on Image Processing*, Vol. 7, No. 3, 359-369